Applied Catalysis B: Environmental 224 (2018) 553–562

Contents lists available at ScienceDirect

Applied Catalysis B: Environmental

journal homepage: www.elsevier.com/locate/apcatb

Visible light driven water splitting over $CaTiO_3/Pr^{3+}$-Y_2SiO_5/RGO catalyst in reactor equipped artificial gill

Wei Gao[a,b], Wenyan Zhang[a,b,c,**], Bin Tian[a,b], Wenlong Zhen[a,b], Yuqi Wu[a,*], Xuqiang Zhang[a], Gongxuan Lu[a,*]

[a] State Key Laboratory for Oxo Synthesis and Selective Oxidation, Lanzhou Institute of Chemical Physics, Chinese Academy of Science, Lanzhou 730000, China
[b] University of Chinese Academy of Science, Beijing 10080, China
[c] College of Material Engineering, Jinling Institute of Technology, Nanjing, China

ARTICLE INFO

Keywords:
Visible-to-ultraviolet upconversion
Enhanced forward charge transfer over RGO
Inhibition of hydrogen-oxygen reverse recombination reaction by artificial gill
Visible driven overall water splitting
$CaTiO_3$ photocatalyst

ABSTRACT

In this work, the enhanced charge transfer in $CaTiO_3/Pr^{3+}$-Y_2SiO_5/RGO catalyst was achieved by assembled RGO with $CaTiO_3$ and Pr^{3+}-Y_2SiO_5 in visible light driven water splitting. By taking advantage of upconversion luminescence material Pr^{3+}-Y_2SiO_5 (Pr^{3+}-YSO), visible light was upconverted into UV light and was used to excite UV responded nano-$CaTiO_3$ to form charge pairs. Then the efficient forward charge transfer to hydrogen generation site Pt was fulfilled over RGO. Longer life time of charges was confirmed by fluorescence spectra in this catalyst. Simultaneously, removing nascent formed oxygen from reaction mixture by an artificial gill significantly inhibited hydrogen–oxygen reverse recombination reaction. By those technologies application, visible-light-driven overall water splitting was accomplished. The photocatalytic activity for hydrogen generation has been raised up to 480% with excellent stability in three recycle reactions. This photocatalyst system is efficient for visible overall split water over UV-responsive photocatalysts.

1. Introduction

Photocatalytic hydrogen evolution from overall water splitting is one of the most promising ways to store the solar energy, which could help resolve the energy and environmental pollution problems caused by over-consumption of fossil fuels [1–38]. The overall photocatalytic water splitting process involves two half reactions, an oxygen evolution reaction (OER) and a hydrogen evolution reaction (HER). Currently, many semiconductor materials have been used as photocatalysts in hydrogen evolution reaction. Some semiconductor materials capable utilizing visible light have been reported, such as CdS [39], CdSe [40], $InNbO_4$ [41], $BiVO_4$ [42], Bi_2MoO_6 [43], Bi_2WO_6 [44], TaON [45], g-C_3N_4 [46], $(Ga_{1-x}Zn_x)(N_{1-x}O_x)$ [47], but some of these photocatalysts are unstable during the reaction due to the photocorrosion [48–51]. Other semiconductors, such as TiO_2 [52–54] and $SrTiO_3$ [55–57], are stable and efficient for hydrogen evolution but only match the UV light in the solar spectrum. Consequently, developing efficient photocatalysts with the stable features and fully usage of sunlight are urgently required.

Several methods have been adopted to improve the utilization of sun light, such as doping of metal or nonmetal elements on TiO_2 [54], $SrTiO_3$ [57], semiconductor coupling (CuOx/TiO_2 [58], p-NiO grafted n-TiO_2 [59], Fe_2O_3 modified TiO_2 nanotube arrays [60], heterojunctioned $TiO_2/SrTiO_3$ thin film [61]), and dye sensitization [62–66]. Some oxynitrides and nitrides of transition metals [67–69] showed activities for water splitting under visible light irradiation, but they are unstable under light irradiation [59], resulting from the N^{3-} ions oxidation by photogenerated holes. Z-scheme photocatalysts are potential catalysts for water splitting, for example, Fu et al. [70] designed a 2D $MoSe_2$/graphene/HfS_2 photocatalyst, which showed high performance for overall water splitting. Recently, there have been reports of the combination of upconversion luminescence (UC) agents with UV responded photocatalysts, which allows the use of visible or NIR light sources to excite the catalysis. For example, Li et al. [71] reported Er^{3+}:$Y_3Al_5O_{12}$/TiO_2-Pt photocatalyst to generate hydrogen under visible light irradiation. Guo et al. [72] used $NaYF_4$:Yb^{3+}/CdS/TiO_2 nanoparticles to degrade methyl blue under NIR light irradiation.

One the other hand, water splitting to hydrogen is also impeded by the reverse reaction of the recombination of hydrogen and oxygen molecules over the co-catalysts and photocatalysts [73–86]. It is known

* Corresponding authors.
** Corresponding author at: State Key Laboratory for Oxo Synthesis and Selective Oxidation, Lanzhou Institute of Chemical Physics, Chinese Academy of Science, Lanzhou 730000, China.
E-mail addresses: gxlu@lzb.ac.cn (W. Zhang), wiseyanyan@jit.edu.cn (Y. Wu), yuqiwucas@163.com (G. Lu).

http://dx.doi.org/10.1016/j.apcatb.2017.10.072
Received 18 June 2017; Received in revised form 2 October 2017; Accepted 31 October 2017
Available online 31 October 2017
0926-3373/

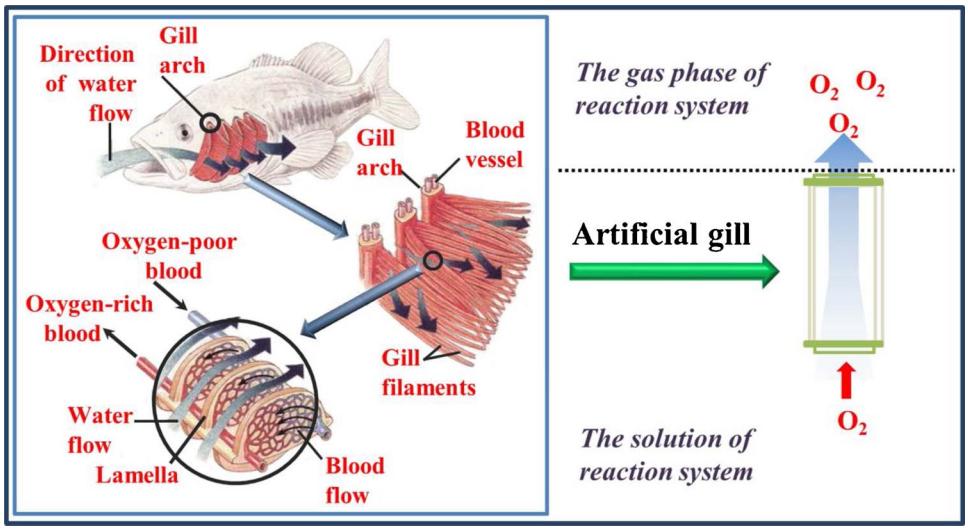

Fig. 1. The structure of fish gill and the schematic diagram of artificial gill.

that about 0.03102 L of oxygen can be dissolved in one liter of water, while only 0.01819 L of hydrogen can be dissolved in one liter of water at 20 °C and 100 kPa. Since the dissolved oxygen is about 1.7 times higher than that of hydrogen in water, the reverse reaction of hydrogen and oxygen recombination occurred very fast over the photocatalysts. As a result, no net hydrogen evolution could be occurred in the semiconductor dispersion. Several strategies have been reported to inhibit this recombination, for example, Takata et al. [86] constructed a hydrated Cr_2O_3 layer over the surface of cocatalyst nanoparticle to hinder the access of evolved O_2 molecules to the surface of the H_2 evolution sites, effectively achieved overall water splitting. We previously reported the inhibition of the reverse hydrogen- oxygen recombination reaction of by adding O_2 transfer reagent hemoglobin [73] and perfluorodecalin [87]. Besides, artificial gill can works as an efficient technologies to remove oxygen from reaction mixture to inhibit this reverse reaction [85].

In this work, we assembled $CaTiO_3/Pr^{3+}$-Y_2SiO_5 with RGO to synthesize a complex photocatalyst $CaTiO_3/Pr^{3+}$-Y_2SiO_5/RGO. Visible light was upconverted into UV light and that UV light was used to excite UV responded nano-$CaTiO_3$ to form charge pairs by taking advantage of upconversion luminescence properties of Pr^{3+}-Y_2SiO_5 (Pr^{3+}-YSO). The enhanced forward charge transfer to hydrogen generation site Pt during water splitting was achieved over RGO. In the same time, removing newly formed oxygen from reaction mixture by an artificial gill significantly inhibited hydrogen-oxygen reverse recombination reaction. By those technologies application, visible-light-driven overall water splitting was accomplished, and the photocatalytic activity for hydrogen generation has been raised up to 480% with excellent stability in three recycle reactions.

2. Experiments

2.1. The preparation of Pr^{3+}-$CaTiO_3$, Pr^{3+}-Y_2SiO_5 and Pr^{3+}-Y_2SiO_5/Pr^{3+}-$CaTiO_3$

The Pr^{3+}-$CaTiO_3$ (Pr^{3+}-CTO), Pr^{3+}-Y_2SiO_5 (Pr^{3+}-YSO) and Pr^{3+}-Y_2SiO_5/Pr^{3+}-$CaTiO_3$ (Pr^{3+}-CTYS) composite were synthesized according to the previous reported method [73]. Typically, the $CaTiO_3$ was synthesized *via* sol-gel method. Details are as follows, 5 mL tetrabutyl titanate (AR) was firstly mixed with 15 mL anhydrous ethanol and the obtained mixture was ultrasonic treated for 30 min, which was named solution A. The corresponding stoichiometric calcium nitrate tetrahydrate (AR) and praseodymium nitrate hexahydrate (AR) were dissolved in 7 mL anhydrous ethanol containing 1 mL distilled water while keeping the molar ratio of Ca:Ti constant 1:1, Pr^{3+}:Ti was 0.002:1 with 0.6 g boric acid as cosolvent, then the mixture was ultrasonic treated until it was completely dissolved to homogeneous solution, which was named solution B. Slowly added solution B to A under stirring, then one or two drops of concentrated HCl were added. The sol was formed quickly after addition solution B to A, then the mixture was kept at room temperature for 90 min under stirring, and dried at 80°C overnight, the obtained powders were calcinated at 1300°C for 4 h, the white color powders which could emit red light under UV light irradiation were finally gained. The similar preparation method was used in Pr^{3+}-Y_2SiO_5 and Pr^{3+}-Y_2SiO_5/Pr^{3+}-$CaTiO_3$ composite photocatalyst preparation, here, yttrium nitrate hexahydrate, praseodymlum nitrate hexahydrate (the percentage of Pr^{3+} was 0.7 mol% to Si), boric acid, anhydrous ethanol and distilled water were mixed together and ultrasonic treated until the mixture was completely dissolved. Then a certain amount of prepared Pr^{3+}-CTO were added to the mixture solution to synthesize Pr^{3+}-CTYS photo-catalysts, maintaining the weight ratio of Pr^{3+}-YSO and Pr^{3+}-CTO was finally around 4:1. The mixture was then stirred at 80 °C in a water bath while about 2 mL ammonia was added at the beginning to accelerate the process of sol formation. Finally, the sol was calcined at 1000 °C for 4 h. The Pr^{3+}-YSO were prepared by the similar method without adding Pr^{3+}-CTO.

2.2. Artificial gill [85]

It is known that fish can extract the dissolved oxygen from the water through the gill in water. The gill structure is shown in Fig. 1. Gills are typical respiratory organ of fish, which consist of gill arch, gill rake, gill filament, gill lamella, etc. Fish exchanges the gas by gill lamella in the water. Gill wall is very thin, and contains a lot of capillaries. One can achieve similar function just using a gas diffusion polymer film, one side is water with dissolved oxygen and another side is bubbled with high pure argon gas. By this way, the oxygen concentration difference leads to oxygen diffusion from water side to the gas side, then the dissolved oxygen in water could be transferred from reaction mixture to gas phase. We applied artificial gill to the photocatalytic overall water splitting system. The continuous argon gas was injected to decrease oxygen concentration in gas side of separation membrane, thus the dissolved oxygen would penetrate the separation membrane and was moved out of the reaction system.

2.3. Photocatalytic H_2 evolution activity

Photocatalytic reactions were carried out in a sealed pyrex flask (190 mL), which has a flat window with the irradiation area about 14 cm^2 at room temperature. In a typical reaction, 100 mg Pr^{3+}-CTYS,

100 μL methanol and different volumes of 5 mg/ml K_2PtCl_6 (keeping Pt loadings at 0.2 wt%, 0.5 wt%, 0.8 wt% and 1 wt%, respectively) were dispersed into 140 mL distilled water in a sealed pyrex flask to lead Pt photoreduction in situ. The mixture was ultrasonic treated 30 min before bubbling Ar gas to degas for 30 min, subsequently the reactor was irradiated under UV light to load Pt on Pr^{3+}-CTYS. During the reduction process, the gas composition and content in the sealed Pyrex flask were monitored by gas chromatography. After the reaction of Pt photoreduction was carried out for 6 h, different amount of RGO (1, 2, 3, 4 and 5 mg) was added to the reaction system with another 300 μL methanol. The mixture was continuously irradiated under UV light to load partial photoreduced Pt on RGO. Subsequently, over 24 h irradiated was needed to completely consume the methanol in reaction system. And the catalyst itself with loaded Pt was ready for the water splitting experiment. The photocatalyst activity of hydrogen evolution was measured under visible light using gas chromatography (Agilent 6820, TCD, 13 × column, Ar carrier). The light source was a 300-W Xenon lamp with a 400 nm cutoff filter.

2.4. Photoelectrochemical measurements

All the photoelectrochemical measurements were carried out on an electrochemical analyzer (CHI660E) in a homemade standard three-electrode cell, consisting of an organic glass enclosure with a quartz window and a 1.2 cm diameter opening opposite the window to the work electrode clamped. The working electrodes were prepared by dropping the catalyst sample directly onto the surface of the precleaned indium tin oxide glass (ITO glass). The area of the working electrode exposed to the electrolyte was about 1 cm^2. Platinum foil was used as counter electrode and a saturated calomel electrode (SCE) as the reference electrode. The current-time curve was obtained under unbiased condition to investigate the anodic photocurrent. The linear sweep voltammetry (LSV) curves were recorded with the scan rate of 1 mV s^{-1}. The excitation source was a 300-W Xenon lamp with a 420 nm cutoff filter.

The apparent quantum efficiency (AQE) was measured under the same photocatalytic reaction conditions with irradiation light through a bandpass filter (400 nm). Photon flux of the incident light was determined using a Ray virtual radiation actinometer (FU 100, silicon ray detector, light spectrum, 400–700 nm; sensitivity, 10–50 μV μm mol^{-1} m^{-2} s^{-1}). The reaction solutions were irradiated for 60 min with bandpass filters for AQE tests on the H_2 production. The following equation was used to calculate the AQE.

$$AQE = \frac{2\times\text{the number ofevolution hydrogenmolecules}}{\text{the number of incidentphotons}} \times 100\%$$

2.5. Isotopes tracer experiment

In order to demonstrate that Pr^{3+}-Y_2SiO_5/Pr^{3+}-$CaTiO_3$/Pt ability as photocatalyst for overall water splitting to hydrogen and oxygen simultaneously, isotopes tracer experiments were carried out. Experimental steps were followed by the method described above, except the distilled water was changed to D_2O or $H_2{}^{18}O$ for the detection of D_2 and $^{18}O_2$. The formed D_2 and $^{18}O_2$ were measured by GC–MS (MAT 271).

2.6. Characterizations of the catalysts

The X-ray photoelectron spectroscopy (XPS) analysis was conducted with a VG Scientific ESCALAB210-XPS photoelectron spectrometer with an Al Kα X-ray resource. X-ray diffraction patterns (XRD) of the samples were recorded on a Rigaku B/Max-RB X-ray diffractometer with a nickel-filtrated Cu Kα radiation, specifically using a position sensitive detector at the step time of 15 s at 40 mA and 40 kV, scan step 0.017°, and the 2θ range was 5–90°. Transmission electron microscopy (TEM) and HRTEM images were obtained using a Tecnai-G2-F30 field emission transmission electron microscope operating at accelerating voltage of 300 kV. The fluorescence spectra were measured using a Hitachi F-4500 fluorescence spectrometer with excitation wavelength at 447 nm, 488 nm, 515 nm and 540 nm respectively. The conversion efficiency of Pr^{3+}-CTYS was conducted with steady state/transient fluorescence spectrometer (FLS920, Edinburgh Instruments) under 447 nm excitation.

3. Results and discussion

Due to its wide band gap, only UV light irradiation could be used by Pr^{3+}-CTO/Pt to catalyze overall water splitting. No hydrogen was detected under visible light irradiation over Pr^{3+}-CTO/Pt itself. We successfully made Pr^{3+}-CTO/Pt active under visible light irradiation by assembling Pr^{3+}-CTO/Pt with Pr^{3+}-YSO and using FDC as oxygen transfer agent [73]. When RGO was introduced, the overall water splitting activity of Pr^{3+}-CTYS/Pt were enhanced, the hydrogen evolution rate was 0.41 μmol g^{-1} in 4 h under visible light irradiation (Fig. 1(a)), which was 2.6 times greater than single Pr^{3+}-CTYS/Pt (0.16 μmol g^{-1}). When artificial gill was used in reactor, the hydrogen evolution rate further reached to 0.77 μmol g^{-1} in 4 h. The synergy between RGO, Pr^{3+}-CTYS/Pt and artificial gill gave the highest activity of overall water splitting under visible light irradiation. This RGO/Pr^{3+}-CTYS/Pt catalyst exhibited stable recycle activity for visible-light-driven HER, and no obvious deactivation was observed after 12 h reaction (Fig. 2(b)), indicating that assembling of Pr^{3+}-YSO not only widened the working spectra of Pr^{3+}-CTO photocatalyst to visible light,

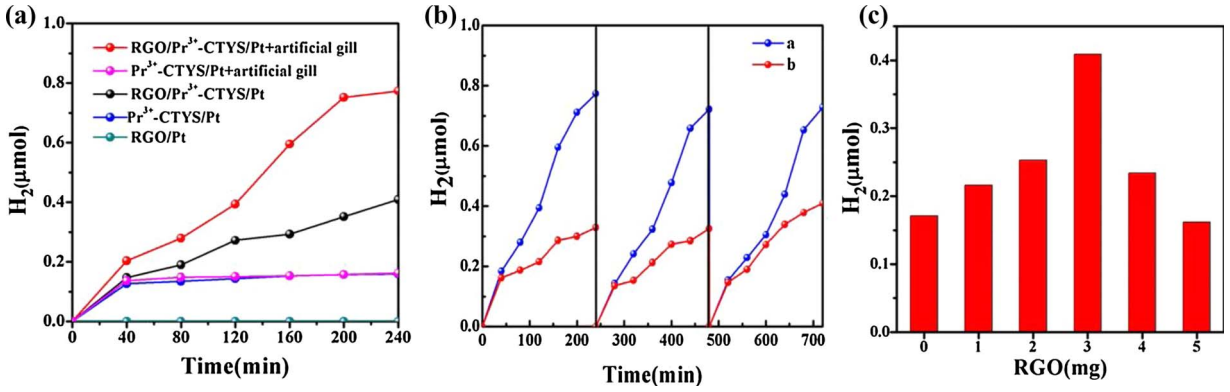

Fig. 2. (a) Photocatalytic activity of Pr^{3+}-CTYS/Pt with and without artificial gill, RGO/Pr^{3+}-CTYS/Pt with and without artificial gill, RGO/Pt under visible light; (b) stability testing of RGO/Pr^{3+}-CTYS/Pt with and without artificial gill corresponding to a and b respectively; (c) maximum H_2 evolution over RGO/Pr^{3+}-CTYS/Pt in the presence of artificial gill with the different amount of RGO(0, 1, 2, 3, 4 and 5 mg respectively).

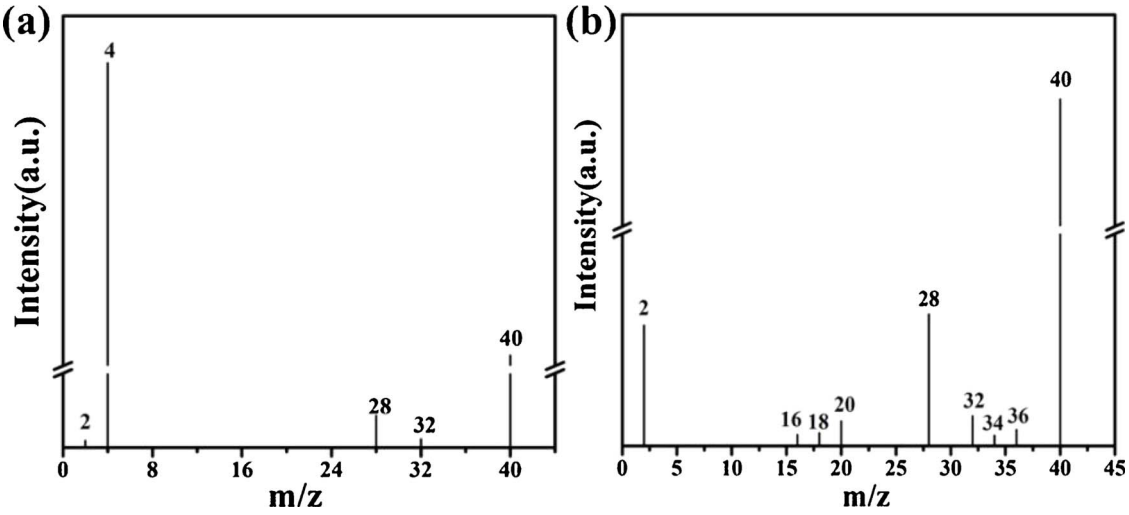

Fig. 3. GC–MS spectra of water splitting gas products in the presence of (a) D_2O and (b) $H^{18}O_2$.

but enhanced the catalyst stability during reaction (Supporting information 1). And the flat band potentials, the VB and CB positions of $CaTiO_3$ and Y_2SiO_5 have been measured and presented in Fig. S3-S4. The influence of the amount of RGO also been studied. With the RGO concentration increasing, the activity of hydrogen generation increased firstly and then decreased as shown in Fig. 2(c), the highest activity was appeared in adding 3 mg RGO. The effects of the amounts of Pr^{3+} and Pt in the catalysts on the performance of water splitting were also investigated and the results were shown in Supporting information. The data about RGO/Pr^{3+}-CTYS were all studied under the optimized doping amount of Pr^{3+} at 0.7 mol% and Pt at 0.5 mol%. The AQE of RGO/Pr^{3+}-CTYS/Pt for hydrogen evolution was 0.003% under 400 nm. Isotopes tracer test was conducted to confirm visible-light-driven hydrogen evolution from pure water. As shown in Fig. 3, D_2 and $^{18}O_2$ were detected when D_2O and $H^{18}O_2$ were used in isotopes tracer test respectively, the results proved that the H_2 and O_2 were generated by photocatalytic water splitting simultaneously. The isotopes tracer test also identified that the RGO/Pr^{3+}-CTYS/Pt was capable of hydrogen evolution triggered by visible light irradiation.

The visible-to-ultraviolet UC capability of Pr^{3+}-YSO is attributed to the excited state absorption (ESA) and energy transfer UC (ETU) process of Pr^{3+} ions in Y_2SiO_5 lattices. In terms of the ESA, a single Pr^{3+} ion was pumped to its excited intermediate state after successively absorbing the energy of two photons (ω_1 and ω_2), and UC fluorescence was released when the excited electron transferred back to the ground state via radiation relaxation. The ^3P_J, $^1I_6$ levels of Pr^{3+} ion can be used as intermediate excited states to achieve the ESA process, like the process of $^3H_4 \rightarrow {}^3P_0 \rightarrow$ 4f5d [88–90]. In the case of ETU process, the energy transfer occurred between two neighboring Pr^{3+} ions (one as the sensitizer and the other as the activator) rather than consecutive absorption of two photons in a single Pr^{3+} ion [91]. Specifically, two Pr^{3+} ions at $^3P_0$ state interact with each other and both of them have absorbed the energy of a photon (ω_1), one Pr^{3+} transfers its energy to the another one by energy transfer (ET) process, so one Pr^{3+} goes back to the $^3H_4$ ground state, while the another one is excited into the 4f5d band for visible-to-ultraviolet UC. Our experiments confirmed this scheme. The capability of RGO/Pr^{3+}-CTYS/Pt for visible-light-driven water splitting is accomplished by the visible-to-ultraviolet UC ability of Pr^{3+}-YSO. As shown in Fig. 4(a–d), the prepared Pr^{3+}-YSO, Pr^{3+}-CTYS/Pt and RGO/Pr^{3+}-CTYS/Pt effectively transfer the visible light of 447 nm, 488 nm, 515 and 540 nm to 253–371 nm UV emission, which can be utilized by Pr^{3+}-CTO/Pt for overall water splitting. The visible-to-ultraviolet UC of Pr^{3+}-YSO was also investigated by transient photocurrent test. As shown in Fig. 4(f), Pr^{3+}-CTO/Pt exhibited no photocurrent under visible light irradiation. When the Pr^{3+}-CTO/Pt was assembled with Pr^{3+}-YSO, Pr^{3+}-CTYS/Pt exhibited obviously enlarged photocurrent under visible light irradiation, which confirmed that incident visible light was converted to UV light by Pr^{3+}-YSO to yield large amounts of photogenerated electrons and holes in Pr^{3+}-CTO. It was note that RGO/Pr^{3+}-CTYS/Pt appeared much higher photocurrent than Pr^{3+}-CTYS/Pt, fully reflected the excellent performance of RGO [92].

Furthermore, the fluorescence lifetimes over Pr^{3+}-CTO, Pr^{3+}-CTYS, Pr^{3+}-CTYS/Pt and RGO/Pr^{3+}-CTYS/Pt were also been investigated. The fluorescence lifetimes were obtained by fitting the decay profiles with two exponential terms. As a long afterglow material, Pr^{3+}-CTO could emit long-time red light around 600 nm under UV light excited (Fig. S6) and possessed long-lifetime photogenerated electrons [93]. According to the PL spectrum of Pr^{3+}-YSO, we chose 341 and 371 nm as excitation wavelength to investigate fluorescence lifetimes of Pr^{3+}-CTO, the corresponding maximum excitation were located at 592 and 597 nm respectively (Fig. 5). In Table 1, the 597 nm emission of 371 nm singlet excited Pr^{3+}-CTO gave the longest lifetime of 52692.83 ns, showing the characteristic of having long-lifetime excitation electrons over Pr^{3+}-CTO in UV light region. When assembled Pr^{3+}-CTO with Pr^{3+}-YSO, that property successfully presented under visible light excitation. We chose 454 nm as excitation wavelength and the mainly emission wavelength at 592 and 597 nm. The Pr^{3+}-CTYS, Pr^{3+}-CTYS/Pt and RGO/Pr^{3+}-CTYS/Pt all showed long fluorescence lifetimes as 98.69, 150.91 and 158.90 ns, respectively. All results indicated that Pr^{3+}-YSO successfully upconverted UV light to Pr^{3+}-CTO under visible light irradiation. But because the low upconversion efficiency (Supporting information 5) [94] the fluorescence lifetimes were not as high as single Pr^{3+}-CTO under UV light excitation, which still much higher than general semiconductor materials [95]. The presence of graphene sheets effectively enhance the electron transfer rate and prevent the recombination processes in such a way that fast electron transfer and a spatial separation of electrons could be achieved. Those photogenerated carriers then facilitated the HER and OER simultaneously over Pr^{3+}-CTO/Pt. And accompanied with artificial gill, we finally achieved the simultaneous evolution of hydrogen and oxygen. Pt nanoparticles coupled with RGO effectively prolong the electrons lifetime of Pr^{3+}-CTYS, which resulting in a higher hydrogen evolution rate.

We then investigated the chemical state of RGO in RGO/Pr^{3+}-CTYS/Pt photocatalyst. Raman spectrum is regarded as an efficient tool for the characterization of carbon nanomaterials particularly graphene, and Fig. 6(a) showed the Raman spectrum of GO and RGO/Pr^{3+}-CTYS/Pt. Raman spectrum of GO showed the peaks at 1335 and 1595 cm^{-1} which were typical D and G bands respectively. The G band was the characteristics of all sp^2 carbon forms and provided the information on

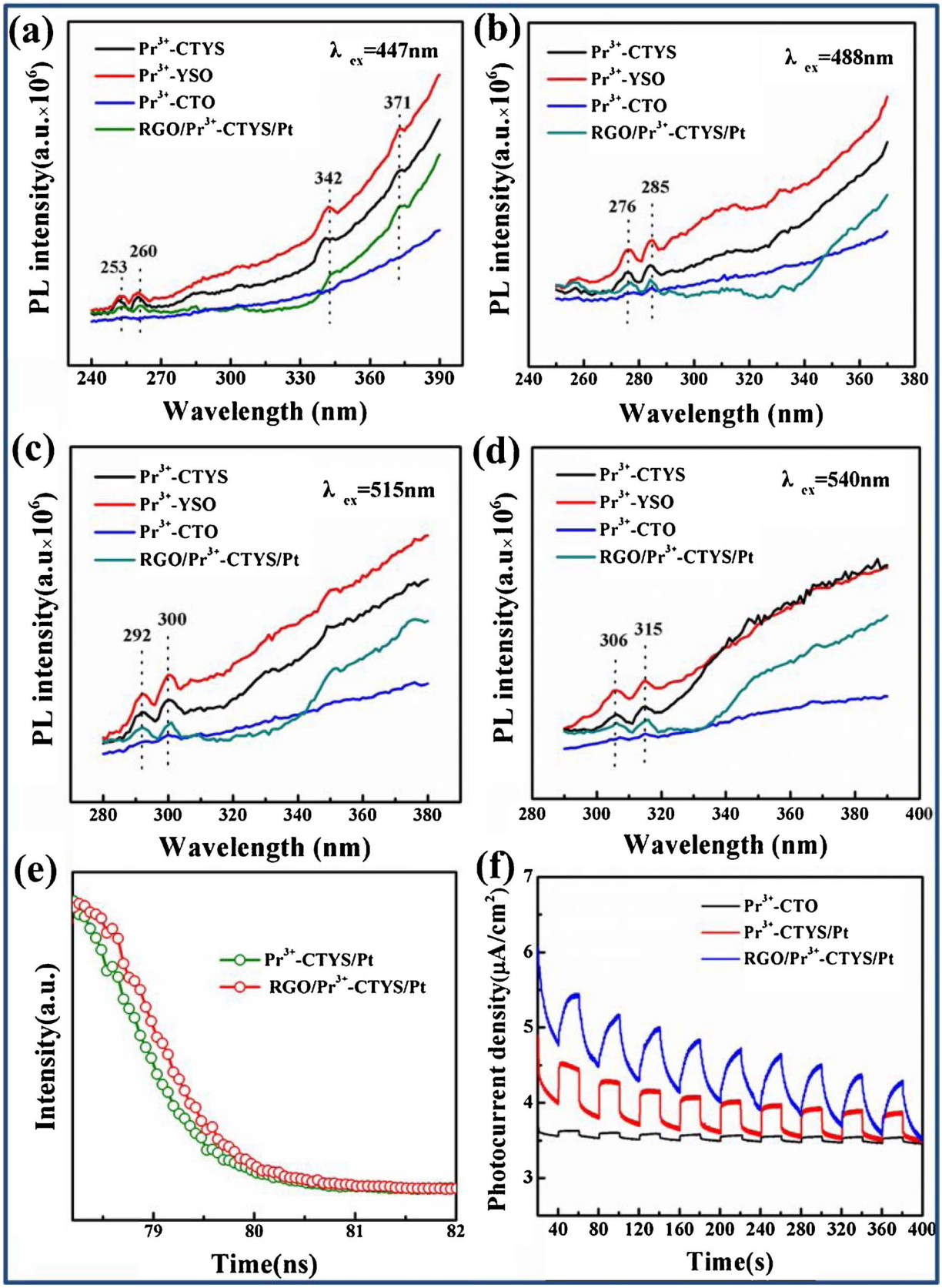

Fig. 4. (a–d) The photoluminescence (PL) spectra of the Pr^{3+}-YSO, Pr^{3+}-CTO, Pr^{3+}-CTYS/Pt and RGO/Pr^{3+}-CTYS/Pt under different excitation wavelength; (e) the time-resolved photoluminescence (TRPL) spectra of Pr^{3+}-CTYS/Pt and RGO/Pr^{3+}-CTYS/Pt at an excitation wavelength of 454 nm. (f) Transient photocurrent – time curves of Pr^{3+}-CTO/Pt, Pr^{3+}-CTYS/Pt and RGO/Pr^{3+}-CTYS/Pt under visible light irradiation.

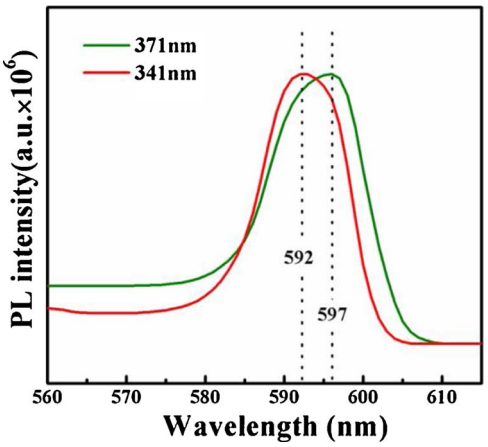

Fig. 5. The emission spectra of the Pr^{3+}-CTO under 341 and 371 nm excitation.

in-plane vibration of the sp^2 carbon atoms [96,97]. The D band was an indication of disorder of GO indicating the presence of sp^3 defects [98,99]. The intensity ratio (I_D/I_G) of D band to G band of the GO before reaction was about 1.07 (Fig. 6ii). After forming RGO/Pr^{3+}-CTYS/Pt the ratio decreased to 0.81 (Fig. 6i). This suggests that the defects on the GO surface decreased might result from the reduction of carboxyl, as a return the forming RGO/Pr^{3+}-CTYS/Pt effectively increased the hydrogen evolution rate due to the excellent performance of RGO. To shed more light on the existence state of RGO, we examined the charged nature of C in the RGO/Pr^{3+}-CTYS/Pt by XPS experiments and shown in Fig. 6(b). The main peak at 284.7 eV was assigned to sp^2-hybridized graphite-like carbon (C—C sp^2), and the peaks centered at 286.0 and 289.3 eV were attributed to surface oxygen groups (designated as C—O—C and O—C═O, respectively) [100–102]. Furthermore, it was found that the surface oxygen functional groups relative content on RGO/Pr^{3+}-CTYS/Pt lower than GO (Fig. S8), which was consistent with the Roman results.

According to the results above, we demonstrated the mechanism of RGO/Pr^{3+}-CTYS/Pt used for photocatalytic hydrogen evolution in Scheme 1. Firstly visible light was captured by Pr^{3+}-YSO and successfully passed UV light to Pr^{3+}-CTO/Pt through upconvension process to generate long-lifetime electrons and holes. Then the excited electrons participated in the hydrogen evolution reaction. Specifically, part of the excited electrons directly transferred to Pt nanoparticles on Pr^{3+}-CTYS to reduce protons to hydrogen as shown in unit A_1. Another part of the electrons were input to RGO, then the protons were reduced to hydrogen on Pt over RGO surface as illustrated in Scheme 1B. Specifically,

Table 1
Decay parameters of Pr^{3+}-CTO, Pr^{3+}-CTYS, Pr^{3+}-CTYS/Pt and RGO/Pr^{3+}-CTYS/Pt in deionized water.

Systems	Ex (nm)	Em (nm)	Lifetime (τ) (ns)	Pre-exponential factors B	Average Lifetime, (τ) (ns)[a]	χ^2
Pr^{3+}-CTO	341	592	τ_1 = 28025.51 τ_2 = 84.24	B1 = 2.402E-05 B2 = 0.883	334.83	1.153
	371	597	τ_1 = 278.20 τ_2 = 74021.46	B1 = 0.216 B2 = 1.995E-03	52692.83	1.048
Pr^{3+}-CTYS	454	592	τ_1 = 193.66 τ_2 = 183.53	B1 = −2.914 B2 = 3.442	98.69	1.268
		597	τ_1 = 169.44 τ_2 = 169.14	B1 = −105.942 B2 = 106.546	92.62	1.305
Pr^{3+}-CTYS/Pt	454	592	τ_1 = 190.98 τ_2 = 181.45	B1 = −2.848 B2 = 3.371	104.95	1.327
		597	τ_1 = 261.78 τ_2 = 260.93	B1 = −28.891 B2 = 29.229	150.91	1.454
RGO/Pr^{3+}-CTYS/Pt	454	592	τ_1 = 214.05 τ_2 = 212.43	B1 = −17.1509 B2 = 17.5865	120.58	1.210
		597	τ_1 = 273.62 τ_2 = 272.15	B1 = −17.7062 B2 = 18.0329	158.90	1.082

[a] Average lifetime < τ > was determined according to reported method.

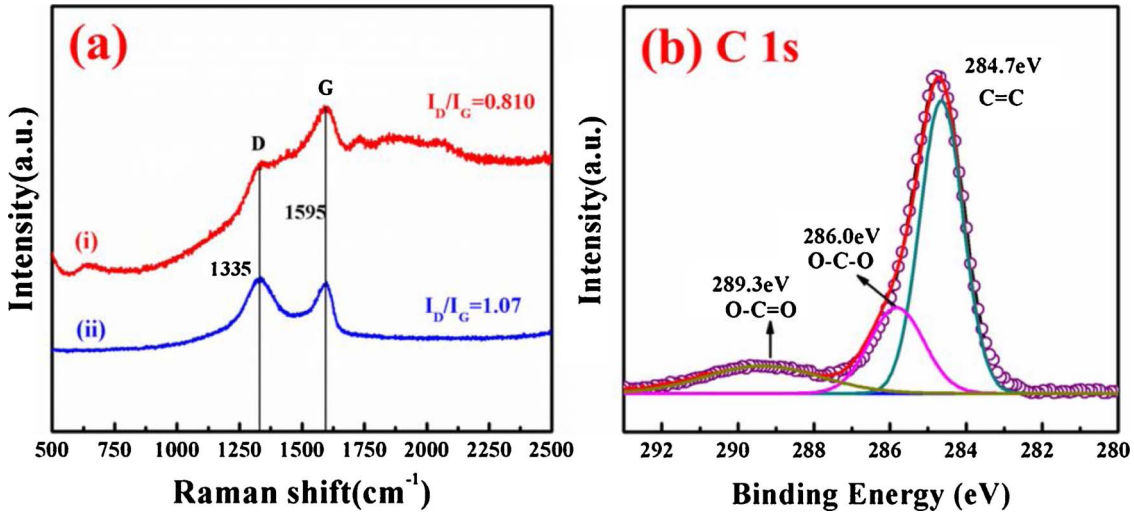

Fig. 6. The Raman spectrum of RGO/Pr^{3+}-CTYS/Pt and RGO, respectively noted as (i) and (ii); (b) C 1s XPS spectrum of RGO/Pr^{3+}-CTYS/Pt.

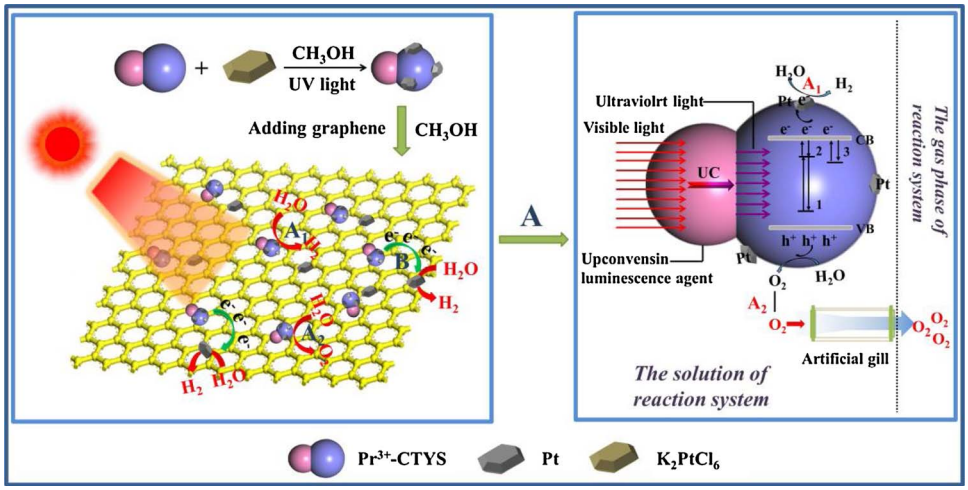

Scheme 1. Visible-light-driven overall water splitting over RGO/Pr^{3+}-CTYS/Pt syetem.

the introducing of RGO added another path for electrons transfer and could be marked as Pr^{3+}-CTYS → RGO → Pt (on RGO). This process effectively facilitated the transfer of electrons, suppressed the recombination of electron-holes and enhanced the utilization rate of photoexcited elections, which significantly increased the overall water splitting activity of Pr^{3+}-CTYS/Pt. Meanwhile, the holes on the valence band of Pr^{3+}-CTO joined in the oxygen evolution reaction. We enlarged the unit A in Scheme 2, clearly exhibited the photocatalytic process on Pr^{3+}-CTYS/Pt. Though the generated electrons and holes were effectively separated by the special excitation process of Pr^{3+}-CTO and excellent conductive property of RGO, the recombination of hydrogen and oxygen still obstructed the release of hydrogen.

Generally, about 0.03102L of oxygen can be dissolved in one liter of water, while only 0.01819L of hydrogen can be dissolved in one liter of water at 20 °C and 100 kPa. Since the dissolved oxygen is about 1.7 times higher than that of hydrogen in water, the reverse reaction of hydrogen and oxygen recombination occurred very fast over the photocatalysts [72,73]. We identified that this reverse recombination reaction also occurred in our Pr^{3+}-CTYS/Pt dispersion (Fig. 7). Before the reaction, the desired amount of hydrogen was injected into the reaction. The concentration of hydrogen in the reactor decreased very significantly in the absence of RGO and artificial gill. That indicated that the newly formed hydrogen would react with dissolved oxygen in water or photocatalytic formed oxygen to H_2O again over catalyst surface if the hydrogen and oxygen recombination process could not be inhibited. In this case, no hydrogen could be detected under irradiation.

Besides, LSV tests shows that the RGO/Pr^{3+}-CTYS/Pt photocatalysts exhibit lower hydrogen evolution potential than Pr^{3+}-CTYS/Pt and Pr^{3+}-CTO/Pt in turn (Fig. 7), indicating that hydrogen are more liable to be generated from over RGO/Pr^{3+}-CTYS/Pt catalyst. That will lead to more serious hydrogen and oxygen recombination at the same time over this composite photocatalyst. Without doubt, the recombination of hydrogen and oxygen is another key obstacle in improving the efficiency of photocatalytic overall water splitting, and is necessary to be inhibited. To fulfill that purpose, unit A_2 (Scheme 2) was used to transfer the photogenerated oxygen molecules away from the photocatalysts. Herein, artificial gill was selected as an oxygen transfer suit to capture the photogenerated oxygen, due to its similar function as fish gills. Our experiments confirmed that using of artificial gill could effectively prevent the hydrogen and oxygen from recombination, as shown in Fig. 7(a) the recombination rates over Pr^{3+}-CTYS/Pt, RGO/Pr^{3+}-CTYS/Pt with artificial gill decreased. Thereafter, the HER and OER were effectively promoted over the RGO/Pr^{3+}-CTYS/Pt photocatalyst and visible-light-driven overall splitting water were achieved.

More detailed investigation was conducted to reveal more intrinsic properties of RGO/Pr^{3+}-CTYS/Pt photocatalyst in visible-light-driven water splitting. In order to reveal the junctions among RGO/Pr^{3+}-CTYS/Pt, we tested the TEM, HRTEM and element mapping of Pr^{3+}-

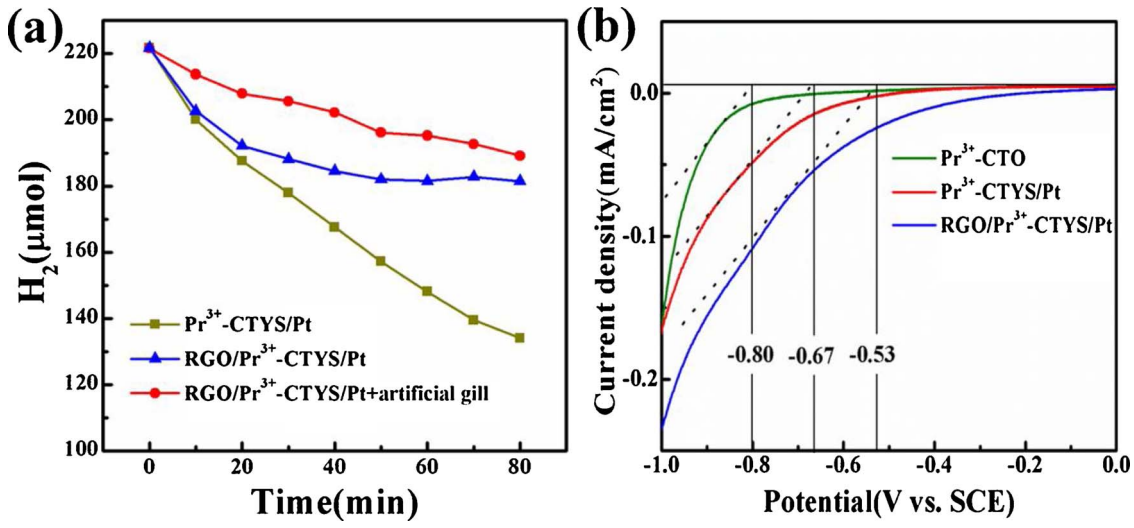

Fig. 7. (a) The hydrogen recombination reaction curves over Pr^{3+}-CTYS/Pt, RGO/Pr^{3+}-CTYS/Pt with and without artificial gill and (b) LSV curves of CTO/Pt, Pr^{3+}-CTYS/Pt and RGO/Pr^{3+}-CTYS/Pt photocatslysts on ITO glass.

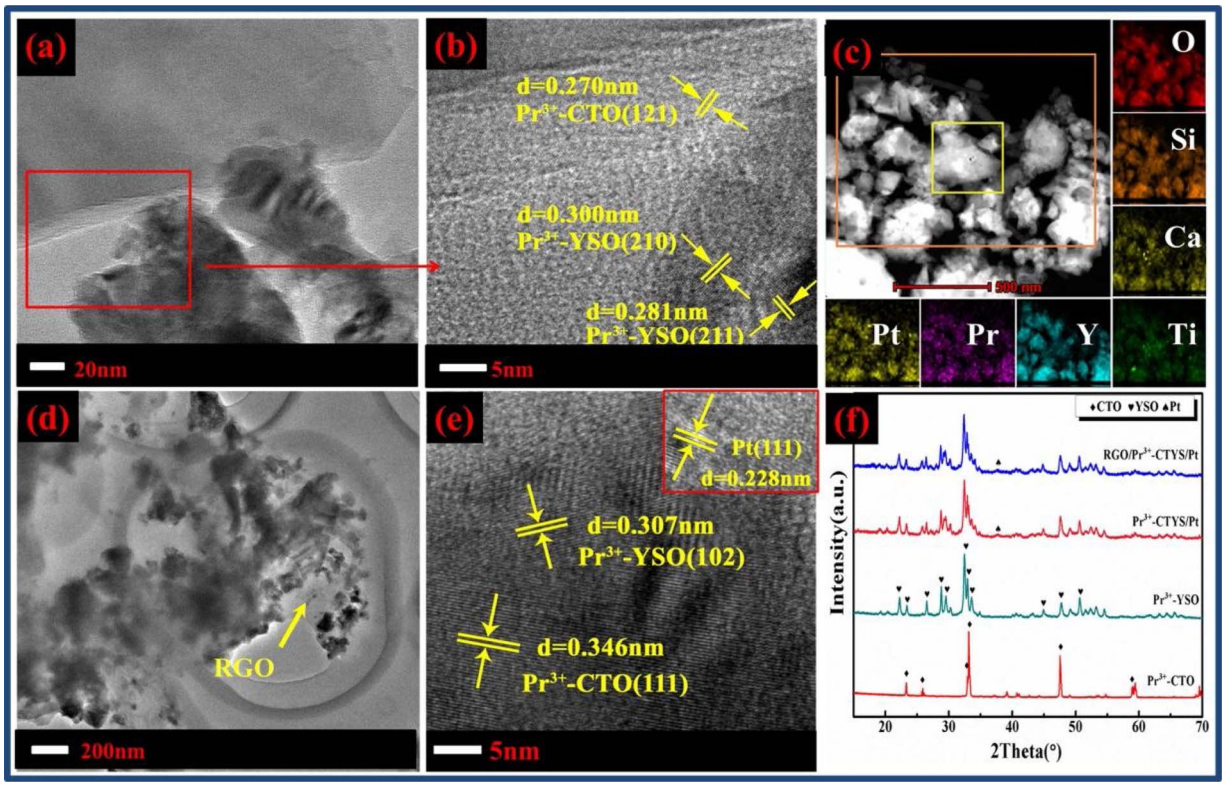

Fig. 8. (a) TEM image of Pr^{3+}-CTYS; (b) HRTEM image of Pr^{3+}-CTYS; (c) Element mapping images of Pr3 + -CTYS; (d)TEM image of RGO Pr^{3+}-CTYS/Pt, (e) HRTEM image of RGO Pr^{3+}-CTYS/Pt; (f) XRD spectrum of Pr^{3+}-CTO, Pr^{3+}-YSO, Pr^{3+}-CTYS/Pt and RGO/Pr^{3+}-CTYS/Pt.

CTYS, RGO/Pr^{3+}-CTYS/Pt and results were presented in Fig. 8. According to the analysis of lattice spacing in Fig. 8(b), we concluded that the Pr^{3+}-CTYS was composed of Pr^{3+}-YSO and Pr^{3+}-CTO, and the two parts were combined together. Furthermore, in Fig. 8(c), the element mapping of Pr^{3+}-CTYS showed that all the elements of Pr^{3+}-YSO and Pr^{3+}-CTO distributed homogeneously in Pr^{3+}-CTYS. Therefore we demonstrated that the Pr^{3+}-YSO and Pr^{3+}-CTO were well connected in Pr^{3+}-CTYS, which promoted Pr^{3+}-YSO delivering the UV light to Pr^{3+}-CTO to generated electrons. When adding RGO and Pt to Pr^{3+}-CTYS, the similar homogeneous distribution of all elements could be seen in element mapping images (Fig. S9). Due to the low concentration of Pt, we could only find RGO in Fig. 8(d), but the Pt (111) clearly existed according to HRTEM in Fig. 8(e). All the analysis illustrated that Pr^{3+}-YSO, Pr^{3+}-CTO, RGO and Pt combined together in RGO/Pr^{3+}-CTYS/Pt, which guaranteed the energy transfer between Pr^{3+}-YSO and Pr^{3+}-CTO and the electrons transfer among Pr^{3+}-CTYS, RGO and Pt.

In consistent with TEM results, XRD patterns also show that the typical peaks of $Y_{4.67}(SiO_4)_3O$ (JCPDS# 30-1457) [103] and $CaTiO_3$ (JCPDS# 22-0153) [104] in RGO/Pr^{3+}-CTYS/Pt photocatalyst (Fig. 8(f)). It's worth noting that the active ingredient of Pr^{3+}-YSO was $Y_{4.67}(SiO_4)_3O$ by the XRD and TEM analysis. According to previous study of the calcination temperature and time affect the crystalline form of the Pr^{3+}-YSO, which began to crystallize at 900 °C with X_1-Y_2SiO_5 and transformed completely to X_2-Y_2SiO_5 at 1250 °C [105] and the $Y_{4.67}(SiO_4)_3O$ formed from X_2-Y_2SiO_5. We have synthesized Y_2SiO_5 calcined at 1000 °C for 4 h [73], therefore it was possible to generate $Y_{4.67}(SiO_4)_3O$ during the our experiment. In addition, we can confirm that the $Y_{4.67}(SiO_4)_3O$ still has visible-to-ultraviolet upconvension capability. Due to the small amount of RGO (3 mg) and miscellaneous peaks around 23° of Pr^{3+}-YSO, the typical characteristic peak of RGO [106,107] was not shown on the XRD spectra. But we could clearly find RGO was uniformly wrapped on the Pr^{3+}-CTYS/Pt in Fig. 8(d).

The XPS spectra performed to examine the chemical composition and oxidation state on the Pr^{3+}-YSO, Pr^{3+}-CTO, Pr^{3+}-CTYS and Pr^{3+}-CTYS/Pt, and the interaction of Pr^{3+}-YSO and Pr^{3+}-CTO. The obtained binding energies were corrected for specimen charging by referencing the C1s binding energy to 284.6 eV. The Y, Si, Ca, Ti and Pt elements on the surface of Pr^{3+}-CTYS/Pt originate from the Pr^{3+}-YSO, Pr^{3+}-CTO and Pt NPs, respectively (Figs. 9 and 10). The Pr 3d XPS shows that the Pr element mainly exist as Pr^{3+} chemical states, which could yield the visible-to-ultraviolet UC in YSO lattices (Fig. 10(a)). In addition, in RGO/Pr^{3+}-CTYS/Pt, the Pr^{3+}-YSO contact closely with Pr^{3+}-CTO to form Pr^{3+}-CTYS heterojunction (Fig. 8(a)). Ti 2p XPS and Si 2p XPS spectra confirm the formation of Pr^{3+}-CTYS heterojunction (Fig. 10(c) and (d)). After assembling Pr^{3+}-CTO with Pr^{3+}-YSO, the Ti $2p_{3/2}$ and Ti $2p_{1/2}$ binding energies appeared no obvious different, when combined with RGO the Ti $2p_{3/2}$ blue shift from 458.3 eV to 458.6 eV, Ti $2p_{1/2}$ binding energies shift from 464.2 eV to 464.6 eV. And the Si 2p binding energies shift higher to 102.1 eV. Those blue shifts of Ti and Si

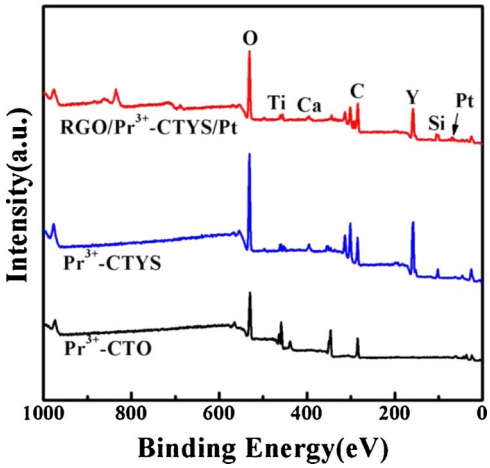

Fig. 9. XPS survey of Pr^{3+}-CTO, Pr^{3+}-CTYS and RGO/Pr^{3+}-CTYS/Pt.

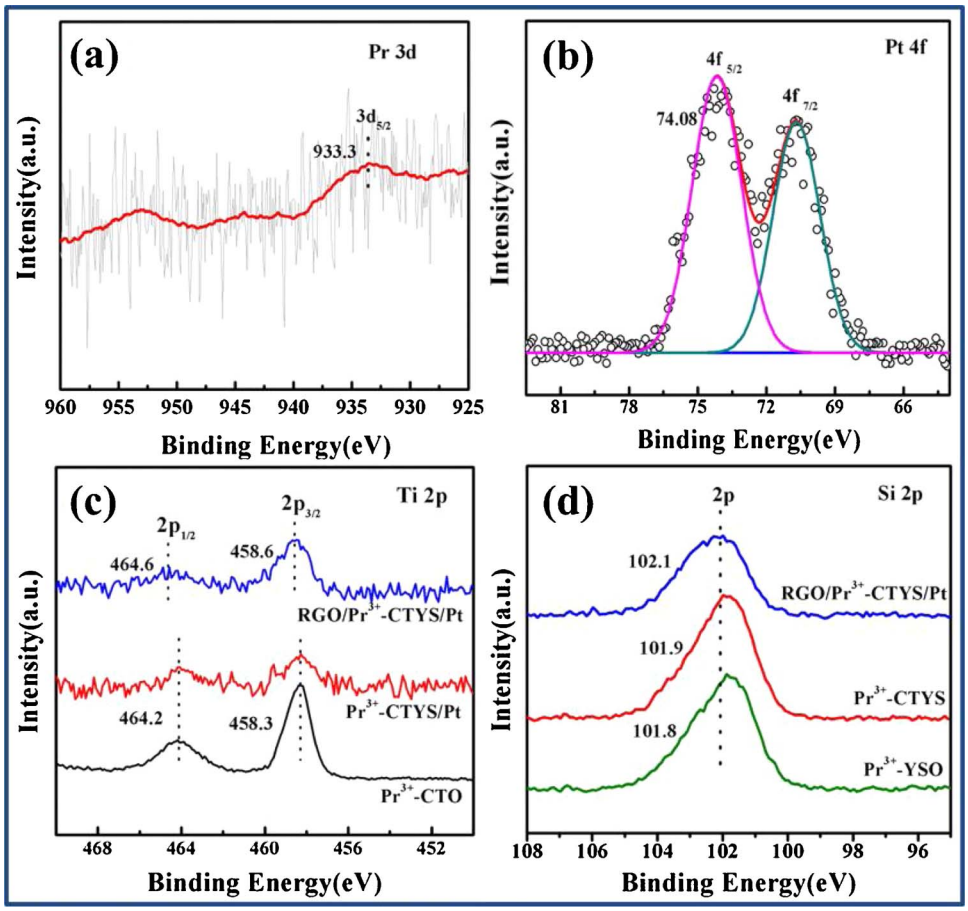

Fig. 10. (a) Pr 3d XPS of RGO/Pr^{3+}-CTYS/Pt and (b) Pt 4f XPS of RGO Pr^{3+}-CTYS/Pt; (c) Ti 2p XPS spectra Pr^{3+}-CTO, Pr^{3+}-CTYS/Pt and RGO/Pr^{3+}-CTYS/Pt and (d) Si 2p XPS spectra of Pr^{3+}-YSO, Pr^{3+}-CTYS/Pt and RGO/Pr^{3+}-CTYS/Pt.

binding energy indicated the strong interaction and overlapping electron cloud were generated on the heterojunction between Pr^{3+}-CTO and Pr^{3+}-YSO. And the Pr^{3+}-CTYS/Pt catalyst has a strong interaction with RGO to achieve effectively electrons transfer between them. Moreover, as Pr, Y and Si elements distributed homogeneously on Pr^{3+}-CTO photocatalysts(Fig. 8(f)), indicating the Pr^{3+}-YSO dispersed uniformly on the surface of Pr^{3+}-CTO to form large portions of Pr^{3+}-CTYS heterojunctions, through which the energy and carriers could be transferred effectively between them. Consequently, the UV light generated by Pr^{3+}-YSO could be used better by Pr^{3+}-CTO for overall splitting water. Pt nanoparticles (NPs) mainly exist as metallic state (Fig. 10(b), Pt 4f XPS), and they exposed their high-energy (111) planes in Pr^{3+}-CTYS/Pt (Fig. 8(e)). The metallic Pt NPs are capable of promoting photogenerating hydrogen with lower the HER over-potential for Pr^{3+}-CTYS/Pt photo-catalysts. Paradoxically, photogenerated hydrogen and oxygen are prone to recombine on those metallic Pt NPs. As a result, the application of artificial gill oxygen transfer reagents is indispensable in our reactive system to transfer newly generated O_2 for visible-light-driven overall splitting water.

4. Conclusion

The strategy of combining Pr^{3+}-CTO with the visible-to-ultraviolet upconversion unit provided a new idea for photocatalysis preparation. The visible-to-ultraviolet UC unit on the photocatalyst was able to transfer incident visible radiation to UV light emission. Owing to large area of heterojunction constructed between the visible-to-ultraviolet UC unit and UV-responsive photocatalyst, the UV light yielded from the visible-to-ultraviolet UC unit was utilized successfully by the UV-responsive photocatalyst for overall water splitting. Moreover, the RGO greatly facilitated the forward electron transfer from photoexcited Pr^{3+}-CTO to Pt co-catalyst and suppressed back electron transfer, which significantly enhanced photocatalytic efficiency for H_2 evolution. In addition, the oxygen transfer reagent artificial gill effectively captured and transported photogenerated oxygen away from the photocatalyst surface, thus preventing the nascent generated hydrogen and oxygen from recombining. The synergy effect between RGO, Pr^{3+}-CTYS/Pt and artificial gill help us achieving photocatalytic hydrogen evolution from pure water. This study inspires the utilization of UV-responsive materials to realize overall split water by visible light irradiation.

Notes

The authors declare no competing financial interest.

Acknowledgment

This work is supported by the NSF of China (21433007, 21673262).

Appendix A. Supplementary data

Supplementary data associated with this article can be found, in the online version, at http://dx.doi.org/10.1016/j.apcatb.2017.10.072.

References

[1] M.S. Dresselhaus, I.L. Thomas, Nature 414 (2001) 332–337.
[2] W.P. Wang, G.X. Lu, Prog. Chem. 15 (2003) 74–78.
[3] X.J. Zhang, Z.L. Jin, Y.X. Li, S.B. Li, G.X. Lu, J. Power Source 166 (2007) 74–79.
[4] Z.K. Li, X. Hu, L.J. Zhang, S.M. Liu, G.X. Lu, Appl. Catal. A 417 (2012) 281–289.
[5] G.X. Lu, H.X. Gao, J.S. Suo, S.B. Li, Chem. Commun. 21 (1994) 2423–2424.
[6] W.P. Wang, G.X. Lu, Catal. Lett. 81 (2002) 63–68.
[7] G.X. Lu, B. Tian, J. Mol. Catal. (China) 31 (2017) 101–104.

[8] G.X. Lu, W.L. Zhen, J. Mol. Catal. (China) 31 (2017) 299–304.
[9] K. Ni, L. Chen, G.X. Lu, Electrochem. Commun. 10 (2008) 1027–1030.
[10] Z. Li, Q. Wang, C. Kong, Y. Wu, Y. Li, G. Lu, J. Phys. Chem. C 119 (2015) 13561–13568.
[11] E.T. Cui, G.X. Lu, Int. J. Hydrogen Energy 39 (2014) 8959–8968.
[12] E.T. Cui, G.X. Lu, Int. J. Hydrogen Energy 39 (2014) 7672–7685.
[13] C. Kong, S.X. Min, G.X. Lu, Int. J. Hydrogen Energy 39 (2014) 4836–4844.
[14] S.X. Min, G.X. Lu, Int. J. Hydrogen Energy 38 (2013) 2106–2116.
[15] G.X. Lu, W.Y. Zhang, J. Mol. Catal. (China) 31 (2017) 401–410.
[16] X.X. Zhao, G.X. Lu, Int. J. Hydrogen Energy 41 (2016) 13993–14002.
[17] E.N. Savinov, G.X. Lu, V.N. Parmon, React. Kinet. Catal. Lett. 48 (1992) 553–560.
[18] X.X. Zhao, G.X. Lu, Int. J. Hydrogen Energy 41 (2016) 3349–3362.
[19] C. Kong, Z. Li, G.X. Lu, Int. J. Hydrogen Energy 40 (2015) 9634–9641.
[20] Z. Li, C. Kong, G.X. Lu, Int. J. Hydrogen Energy 40 (2015) 9061–9068.
[21] C. Kong, Z. Li, G.X. Lu, Int. J. Hydrogen Energy 40 (2015) 5824–5830.
[22] X. Hu, D.H. Dong, L.J. Zhang, G.X. Lu, Catal. Commun. 55 (2014) 74–77.
[23] W.Y. Zhang, S.L. Yang, J. Li, W. Gao, Deng Y.B. Deng, W.P. Dong, C.J. Zhao, G.X. Lu, Appl. Catal. B. 206 (2017) 89–103.
[24] R.D. Cortright, R.R. Davda, J.A. Dumesic, Nature 418 (2002) 964–967.
[25] W.Y. Zhang, C. Kong, G.X. Lu, Chem. Commun. 51 (2015) 10158–10161.
[26] W.Y. Zhang, C. Kong, W. Gao, G.X. Lu, Chem. Commun. 52 (2016) 3038–3041.
[27] B. Li, W. Zhen, G. Lu, J. Ma, J. Mol. Catal. (China) 29 (2015) 152–163.
[28] G. Lu, S. Zhang, G. Hou, F. Shi, T. Li, X. Yao, H. Liang, J. Mol. Catal. (China) 30 (2016) 383–390.
[29] G.X. Lu, S.B. Li, Int. J. Hydrogen Energy 17 (1992) 767–770.
[30] S.X. Min, F. Wang, G.X. Lu, Catal. Commun. 80 (2016) 28–32.
[31] X.Q. Zhang, G.X. Lu, Carbon 108 (2016) 215–224.
[32] Z. Li, C. Kong, G.X. Lu, J. Phys. Chem. C 120 (2016) 56–63.
[33] B. Tian, Z. Li, W.L. Zhen, G.X. Lu, J. Phys. Chem. C 120 (2016) 6409–6415.
[34] Z. Li, Y.Q. Wu, G.X. Lu, Appl. Catal. B 188 (2016) 56–64.
[35] Z.L. Jin, G.X. Lu, Energy Fuel 19 (2005) 1126–1132.
[36] Z.X. Huang, Y.F. Li, Y.X. Li, X.Q. Huang, J. Mol. Catal. (China) 31 (2017) 181–187.
[37] J.J. Hou, Q.H. Zhao, G. Li, P.W. Li, J. Hu, J. Mol. Catal. (China) 31 (2017) 258–266.
[38] X.S. Huang, Y.X. Zhao, G.X. Lu, Z.C. Tang, J. Mol. Catal. (China) 31 (2017) 287–298.
[39] Z. Gao, N. Liu, D. Wu, W. Tao, F. Xu, K. Jiang, Appl. Surf. Sci. 258 (2012) 2473–2478.
[40] W.C. Oh, M. Chen, K. Cho, C. Kim, Z. Meng, L. Zhu, Chin. J. Catal. 32 (2011) 1577–1583.
[41] X. Zhang, X. Quan, S. Chen, H. Yu, Appl. Catal. B Environ. 105 (2011) 237–242.
[42] Y. Fu, X. Sun, X. Wang, Mater. Chem. Phys. 131 (2011) 325–330.
[43] F. Zhou, R. Shi, Y. Zhu, J. Mol. Catal. A Chem. 340 (2011) 77–82.
[44] E. Gao, W. Wang, M. Shang, J. Xu, Phys. Chem. Chem. Phys. 13 (2011) 2887–2893.
[45] R. Abe, M. Higashi, K. Domen, J. Am. Chem. Soc. 132 (2010) 11828–11829.
[46] G.G. Zhang, Z.A. Lan, L.H. Lin, S. Lin, X.C. Wang, Chem. Sci. 7 (2016) 3062–3066.
[47] K. Maeda, K. Teramura, T. Takata, M. Hara, N. Saito, K. Toda, Y. Inoue, H. Kobayashi, K. Domen, J. Phys. Chem. B 109 (2005) 20504–20510.
[48] D. Ke, S. Liu, K. Dai, J. Zhou, L. Zhang, T. Peng, J. Phys. Chem. C 113 (2009) 16021–16026.
[49] S.K. Apte, S.N. Garaje, S.D. Naik, R.P. Waichal, J.O. Baeg, B.B. Kale, Nanoscale 6 (2014) 908–915.
[50] C. Kong, S. Min, G. Lu, ACS Catal. 4 (2014) 2763–2769.
[51] T. Mahvelati-Shamsabadi, E.K. Goharshadi, Ultrason. Sonochem. 34 (2017) 78–89.
[52] Y.Q. Wu, G.X. Lu, S.B. Li, J. Photochem. Photobiol. A 181 (2006) 263–267.
[53] H. Lin, C. Shih, Catal. Surv. Asia 16 (2012) 231–239.
[54] H. Lin, C. Shih, J. Mol. Catal. A Chem. 411 (2016) 128–137.
[55] H. Kato, M. Kobayashi, M. Hara, M. Kakihana, Catal. Sci. Technol. 3 (2013) 1733–1738.
[56] T.K. Townsend, N.D. Browning, F.E. Osterloh, ACS Nano 6 (2012) 7420–7426.
[57] W. Chen, H. Liu, X. Li, S. Liu, L. Gao, L. Mao, Z. Fan, W. Shangguan, W. Fang, Y. Liu, Appl. Catal. B 192 (2016) 145–151.
[58] Q. Hu, J. Huang, G. Li, G. Li, J. Chen, Z. Zhang, Z. Deng, Y. Jiang, W. Guo, Y. Cao, Appl. Surf. Sci. 369 (2016) 201–206.
[59] S. Bassaki, H. Niazi, F. Golestani-Fard, R. Naghizadeh, R. Bayati, J. Mater. Sci. Technol. 31 (2015) 355–360.
[60] S. Kuang, L. Yang, S. Luo, Q. Cai, Appl. Fabrication, Surf. Sci. 255 (2009) 7385–7388.
[61] J. Ng, S. Xu, X. Zhang, H. Yang, D. Sun, Adv. Funct. Mater. 20 (2010) 4287–4294.
[62] C. An, S. Peng, Y. Sun, Adv. Mater. 22 (2010) 2570–2574.
[63] K.B. Dhanalakshmi, S. Latha, S. Anandan, P. Maruthamuthu, Int. J. Hydrogen Energy 26 (2001) 669–674.
[64] R. Abe, K. Sayama, H. Arakawa, Chem. Phys. Lett. 362 (2002) 441–444.
[65] R. Abe, K. Hara, K. Sayama, K. Domen, H. Arakawa, J. Photochem. Photobiol. A Chem. 137 (2000) 63–69.
[66] D.J. Martin, P.J.T. Reardon, S.J.A. Moniz, J. Tang, J. Am. Chem. Soc. 136 (2014) 12568–12571.
[67] M. Higashi, K. Domen, R. Abe, Energy Environ. Sci. 4 (2011) 4138–4147.
[68] K. Maeda, T. Takata, M. Hara, N. Saito, Y. Inoue, H. Kobayashi, K. Domen, J. Am. Chem. Soc. 127 (2005) 8286–8287.
[69] H. Fujito, H. Kunioku, D. Kato, H. Suzuki, M. Higashi, H. Kageyama, R. Abe, J. Am. Chem. Soc. 138 (2016) 2082–2085.
[70] C.F. Fu, Q. Luo, X. Li, J. Yang, J. Mater. Chem. A 4 (2016) 18892–18898.
[71] S. Li, Y. Guo, L. Zhang, J. Wang, Y. Li, Y. Li, B. Wang, J. Power Sources 252 (2014) 21–27.
[72] X. Guo, W. Di, C. Chen, C. Liu, X. Wang, W. Qin, Dalton Trans. 43 (2014) 1048–1054.
[73] Z. Li, B. Tian, W.L. Zhen, Y.Q. Wu, G.X. Lu, Appl. Catal. B. 203 (2017) 408–415.
[74] W.L. Zhen, X.F. Ning, B.J. Yang, Y.Q. Wu, Z. Li, G.X. Lu, Appl. Catal. B. 221 (2018) 243–257.
[75] B. Tian, W. Gao, X.Q. Zhang, Y.Q. Wu, G.X. Lu, Appl. Catal. B 221 (2018) 618–625.
[76] Z. Li, B. Tian, W.L. Zhen, W.Y. Zhang, X.Q. Zhang, Y.Q. Wu, G.X. Lu, Appl. Catal. B 219 (2017) 501–510.
[77] X.Q. Zhang, B. Tian, W.L. Zhen, Z. Li, Y.Q. Wu, G.X. Lu, J. Catal. 354 (2017) 258–269.
[78] M. Wang, Z. Li, Y.Q. Wu, J.T. Ma, G.X. Lu, J. Catal. 353 (2017) 162–170.
[79] B. Tian, Z. Li, W.L. Zhen, X.Q. Zhang, G.X. Lu, J. Catal. 352 (2017) 572–578.
[80] E. Lalik, A. Drelinkiewicz, R. Kosydar, R. Tokarz-Sobieraj, M. Witko, T. Szumełda, J. Gurgul, D. Duraczýnska, Appl. Catal. A 517 (2016) 196–210.
[81] H.B. Gao, W.L. Zhen, J.T. Ma, G.X. Lu, Appl. Catal. B 206 (2017) 353–363.
[82] B. Tian, B.J. Yang, J. Li, W.L. Zhen, Y.Q. Wu, G.X. Lu, J. Catal. 350 (2017) 189–196.
[83] Z. Li, B. Tian, W.Y. Zhang, X.Q. Zhang, Y.Q. Wu, G.X. Lu, Appl. Catal. B 204 (2017) 33–42.
[84] W.L. Zhen, F. Gao, B. Tian, P. Ding, Y.B. Deng, Z. Li, H.B. Gao, G.X. Lu, J. Catal. 348 (2017) 200–211.
[85] X. Ning, J. Li, B. Yang, W. Zhen, Z. Li, B. Tian, G. Lu, Appl. Catal. B 212 (2017) 129–139.
[86] T. Takata, C. Pan, M. Nakabayashi, N. Shibata, K. Domen, J. Am. Chem. Soc. 137 (2015) 9627–9634.
[87] W. Gao, W. Zhang, G. Lu, Appl. Catal. B 212 (2017) 23–31.
[88] E.L. Cates, A.P. Wilkinson, J.H. Kim, J. Lumin. 160 (2015) 202–209.
[89] W. Qin, D. Zhang, D. Zhao, Chem. Commun. 46 (2010) 2304–2306.
[90] C. Hu, C. Sun, J. Li, Z. Li, H. Zhang, Z. Jiang, Chem. Phys. 325 (2006) 563–566.
[91] W.Y. Zhang, G.X. Lu, Catal. Sci. Technol. 6 (2016) 7693–7697.
[92] N. Zhang, M.Q. Yang, S. Liu, Y. Sun, Y. Xu, Chem. Rev. 115 (2015) 10307–10377.
[93] P.T. Diallo, K. Jeanlouis, P. Boutinaud, R. Mahiou, J.C. Cousseins, J. Alloy Compd. 323 (2001) 218–222.
[94] E.L. Cates, S.L. Chinnapongse, J.H. Kim, J.H. Kim, Environ. Sci. Technol. 46 (2012) 12316–12328.
[95] W. Zhen, J. Ma, G. Lu, Appl. Catal. B 190 (2016) 12–25.
[96] W. Zhang, J. Cui, C. Tao, Y. Wu, Z. Li, L. Ma, Y. Wen, G. Li, Angew. Chem. Int. 121 (2009) 5978–5982.
[97] J. Lu, J. Yang, J. Wang, A. Lim, S. Wang, K.P. Loh, ACS Nano 3 (2009) 2367–2375.
[98] F. Tuinstra, J.L. Koenig, J. Chem. Phys. 53 (1970) 1126–1130.
[99] A.C. Ferrari, J.C. Meyer, V. Scardaci, C. Casiraghi, M. Lazzeri, F. Mauri, S. Piscanec, D. Jiang, K.S. Novoselov, S. Roth, A.K. Geim, Phys. Rev. Lett. 97 (2006) 187401.
[100] Y. Zhou, Q. Bao, L.A.L. Tang, Y. Zhong, K. Loh, Chem. Mater. 21 (2009) 2950–2956.
[101] L. Zhang, Z. Su, F. Jiang, L. Yang, J. Qian, Y. Zhou, W. Li, M. Hong, Nanoscale 6 (2014) 6590–6602.
[102] P. Chen, T.Y. Xiao, Y.H. Qian, S. Li, S. Yu, Adv. Mater. 25 (2013) 3192–3196.
[103] J. Parmentier, K. Liddell, D.P. Thompson, H. Lemercier, N. Schneider, S. Hampshire, P.R. Bodart, R.K. Harris, Solid State Sci. 3 (2001) 495–502.
[104] C.L. Huang, C.L. Pan, S.J. Shium, Mater. Chem. Phys. 78 (2003) 111–115.
[105] X.M. Han, J. Lin, J. Fu, R.B. Xing, M. Yu, Y.H. Zhou, M.L. Pang, Solid State Sci. 6 (2004) 349–355.
[106] B. Tian, W. Zhen, H. Gao, X. Zhang, Z. Li, G. Lu, Appl. Catal. B 203 (2017) 789–797.
[107] S. Min, G. Lu, Int. Hydrogen Energy 37 (2012) 10564–10574.